

# TESS light curves of $\gamma$ Cas stars

Yaël Nazé<sup>1</sup>,<sup>1</sup>† Gregor Rauw<sup>1</sup> and Andrzej Pigulski<sup>2</sup>

<sup>1</sup>*Groupe d'Astrophysique des Hautes Energies, STAR, Université de Liège, Quartier Agora (B5c, Institut d'Astrophysique et de Géophysique), Allée du 6 Août 19c, B-4000 Sart Tilman, Liège, Belgium*

<sup>2</sup>*Instytut Astronomiczny, Uniwersytet Wrocławski, Kopernika 11, PL-51-622 Wrocław, Poland*

Accepted 2020 August 18. Received 2020 August 18; in original form 2020 July 3

## ABSTRACT

$\gamma$  Cas stars constitute a subgroup of Be stars showing unusually hard and bright X-ray emission. In search for additional peculiarities, we analysed the *TESS* light curves of 15  $\gamma$  Cas analogues. Their periodograms display broad frequency groups and/or narrow isolated peaks, often superimposed over red noise. The detected signals appear at low frequencies, with few cases of significant signals beyond  $5 \text{ d}^{-1}$  (and all of them are faint). The signal amplitudes, and sometimes the frequency content, change with time, even in the absence of outburst events. On the basis of their optical photometric variability,  $\gamma$  Cas stars reveal no distinctive behaviour and thus appear similar to Be stars in general.

**Key words:** stars: early-type – stars: emission line, Be – stars: massive – stars: variables: general.

## 1 INTRODUCTION

Massive stars may display various spectral peculiarities, which is expressed by specific letters being appended to their spectral types. The Be category was introduced to gather stars presenting Balmer hydrogen lines in emission. This emission is now understood as arising in a circumstellar decretion disc (for a review, see Rivinius, Carciofi & Martayan 2013).  $\gamma$  Cas has long been considered as the prototype of this category, but its high-energy properties (high effective temperature and luminosity intermediate between X-ray binaries and ‘normal’ OB stars) appeared at odds with usual observations of massive stars (Jernigan 1976; Mason, White & Sanford 1976; Smith, Lopes de Oliveira & Motch 2016). With time, more than twenty other Oe/Be stars were found to display these peculiarities (Nazé et al. 2020a), leading to the definition of a ‘ $\gamma$  Cas’ subclass amongst Be stars (not linked to the old optical photometric ‘GCAS’ category used in GCVS). The defining criteria of this subclass (Nazé & Motch 2018) are a Be spectral type in the optical range and a thermal X-ray emission with  $\log(L_X(0.5\text{--}10. \text{ keV}) \sim 31.6\text{--}33.2$  (equivalent to  $\log(L_X/L_{\text{BOL}})$  between  $-6.2$  and  $-4$ ) and  $kT > 5 \text{ keV}$  (equivalent to a ratio between the fluxes in the 2.0–10.0 and 0.5–2.0 keV bands larger than 1.6 or to  $L_X(2.0\text{--}10. \text{ keV}) > 10^{31} \text{ erg cm}^{-2} \text{ s}^{-1}$ ) – all X-ray fluxes are after correction for the ISM absorption. When the X-ray data are sufficiently numerous and of high signal-to-noise ratios, two additional characteristics become obvious: the presence of Fe K $\alpha$  fluorescence line near the iron complex at 6.7 keV and variations on both short and long time-scales (Smith et al. 2016; Nazé & Motch 2018). As a comparison point, O-type stars typically show much softer and fainter thermal X-ray emissions, with  $kT \sim 0.6 \text{ keV}$  and  $\log(L_X/L_{\text{BOL}}) \sim -7$  (and B-type stars are even fainter), while X-ray binaries exhibit  $\log(L_X) > 34$ . As not all Be stars have been observed

at X-ray wavelengths, it should be noted that many more cases may remain unidentified at the present time hence the exact incidence of the  $\gamma$  Cas peculiarity remains unknown.

The origin of the  $\gamma$  Cas phenomenon remains debated. Two main scenarios have been proposed, one linked to accretion on to a compact companion (Hamaguchi et al. 2016; Postnov, Oskinova & Torrejón 2017) and another one linked to magnetic star–disc interaction (Smith et al. 2016). In this context, it is important to underline that, up to now, the only reported difference between  $\gamma$  Cas analogues and the other Be stars lies in their X-ray emission. However, not many  $\gamma$  Cas analogues have been the subject of thorough (optical, ultraviolet, infrared) investigations hence important evidence has yet to be identified.

In this context, we decided to investigate the optical variability of  $\gamma$  Cas analogues. Indeed, the variability directly relates to the disc or the star itself hence it could pinpoint their specificities, if the  $\gamma$  Cas phenomenon arises from the Be star and/or its disc. In Nazé et al. (2020b), we already reported the detection of coherent variations from  $\pi$  Aqr and HD 110432 (BZ Cru) while Borre et al. (2020) analysed the case of  $\gamma$  Cas itself. We now extend the study to a larger set of  $\gamma$  Cas analogues. The homogeneous data set provided by *TESS* will constrain the overall characteristics of these stars and help comparing them with other Be stars. Sections 2 and 3 will present the data and their analysis, respectively, while Section 4 puts the results in a broader context. Finally, Section 5 summarizes and concludes this paper.

## 2 DATA REDUCTION AND ANALYSIS

Currently, 25  $\gamma$  Cas stars are known (and references therein Nazé et al. 2020a). We have checked whether they had been observed by the Transiting Exoplanet Survey Satellite (*TESS*) and this was the case of sixteen of them. Amongst these was HD 110432, whose *TESS* light curve was already reported in Nazé et al. (2020b); this paper focuses on the 15 remaining stars but shows HD 110432 again for

\* E-mail: ynaze@uliege.be

† F.R.S.-FNRS Senior Research Associate.

comparison. It may be recalled at this point that *TESS* has a bandpass centered on the classical  $I_c$  filter, but broader as it spans 6000–10 000 Å. It thus records the red and near-infrared emissions of stars.

Four targets were observed at 2 min cadence, and the associated light curves were directly downloaded from the MAST archives.<sup>1</sup> Only the corrected light curves with the best quality (quality flag = 0) data were considered.

For the remaining eleven stars, only *TESS* full frame images (FFI) with 30 min cadence are available. Individual light curves were extracted for each target using the PYTHON package LIGHTKURVE.<sup>2</sup> Aperture photometry was done on image cut-outs of  $50 \times 50$  pixels and using a source mask defined by pixels above a given flux threshold ( $10 e^- s^{-1}$  for most stars, increased to  $15 e^- s^{-1}$  for SAO 49725 and  $\gamma$  Cas and to  $20 e^- s^{-1}$  for V2156 Cyg and HD 119682, to avoid faint neighbours).  $\gamma$  Cas appears saturated in *TESS* images, but the stellar signal is not lost, just spread out on more pixels (the larger aperture may increase the potential contamination from other objects, though). Background, including scattered light, was taken out using a principal component analysis. Furthermore, the data points with errors larger than the mean of the errors plus their  $1\sigma$  dispersion were discarded.

The *TESS* pixel has a size of 21 arcsec and extraction is done over several pixels (the usual aperture has 1–3 px radius), hence crowding issues may arise. Using Simbad, the 2MASS catalogue, and *Gaia*-DR2, we examined whether our 15 targets had neighbours of similar brightness within 1 arcmin radius. Most stars have neighbours that are 3–10 mag fainter, hence their contribution can be considered negligible. Only two stars appear problematic. HD 90563 lies at 37 arcsec of HD 302793 that has a similar brightness and a similar spectral type: it is thus impossible to determine from which star the light variations come. Belonging to NGC 5281, HD 119682 is surrounded by several stars, notably the brighter CPD–62°3559 (K 2 II/III) and HD 119699 (A 1 II). The spectral types of the contaminating objects are in this case different from that of the target, but the *TESS* images revealed that the images of these sources are totally blended, with our target clearly not dominating the output. Since they may not be fully representative of the emissions of the  $\gamma$  Cas stars, the light curves of these two targets should thus be taken with a great caution.

Whatever the cadence, the raw fluxes were converted into magnitudes using  $mag = -2.5 \times \log(flux) + 14$  (constant is arbitrary). Fig. 1 shows the final light curves for each source, including HD 110432 (Nazé et al. 2020b). Two stars (TYC 3681-695-1 and V767 Cen) display strong long-term variations. Their presence leads to large signals at low frequencies that fully hide other information on the photometric behaviour, hence they need to be taken out for our study. The overall trends were determined by averaging the photometric data of these two stars within a 1 d sliding window and then subtracted to get detrended light curves. For TYC 3681-695-1, very rapid changes at  $BJD < 2458791.8$  were further discarded. Three stars ( $\gamma$  Cas, SAO 49725, and V2156 Cyg) were observed in two sectors and the two light curves were combined after comparing their mean flux levels and shifting the second light curve to match the mean level of the first one.

All light curves (individual, detrended, combined) were then analysed using a modified Fourier algorithm adapted to uneven sampling (Heck, Manfroid & Mersch 1985; Zechmeister & Kürster 2009), as there is a small gap in the middle of each sector light curve. Fig. 2 shows the results of these searches, with a 1 per cent

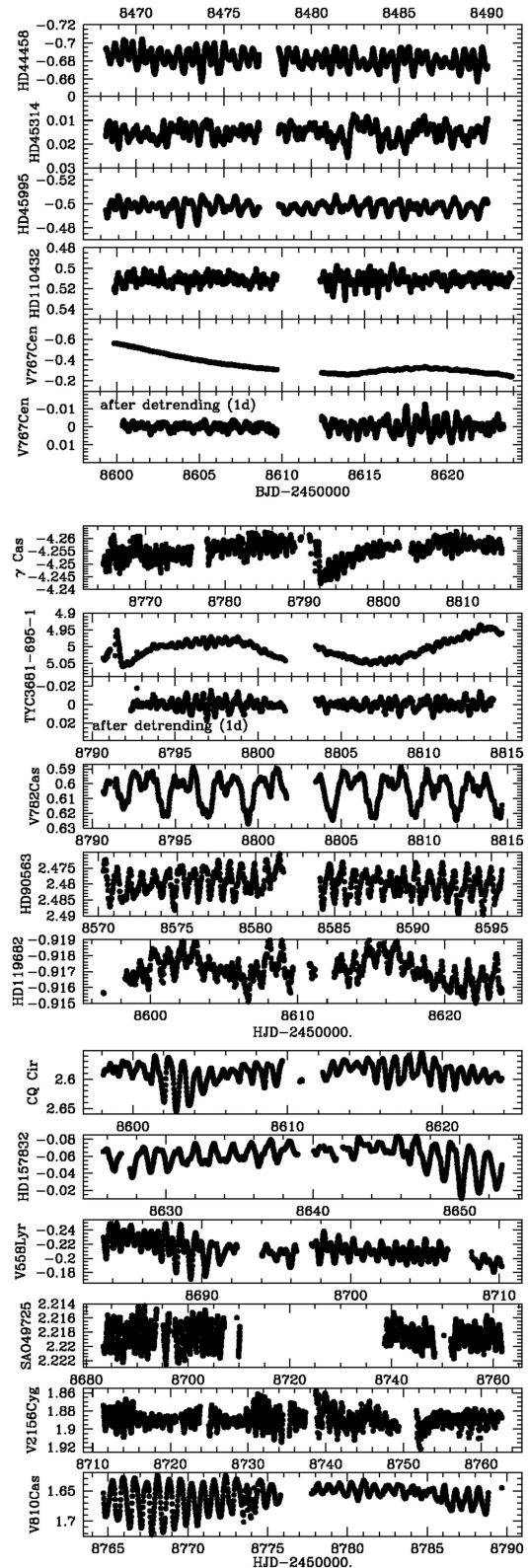


**Figure 1.** *TESS* light curves of the targets, plus HD 110432 for completeness; the ordinate provides magnitudes. In the two cases with a large long-term change, the detrended light curve is also presented. The top five panels present the 2 min cadence light curves, while the middle and bottom panels show data taken with 30 min cadence.

<sup>1</sup><https://mast.stsci.edu/portal/Mashup/Clients/Mast/Portal.html>

<sup>2</sup><https://docs.lightkurve.org/>

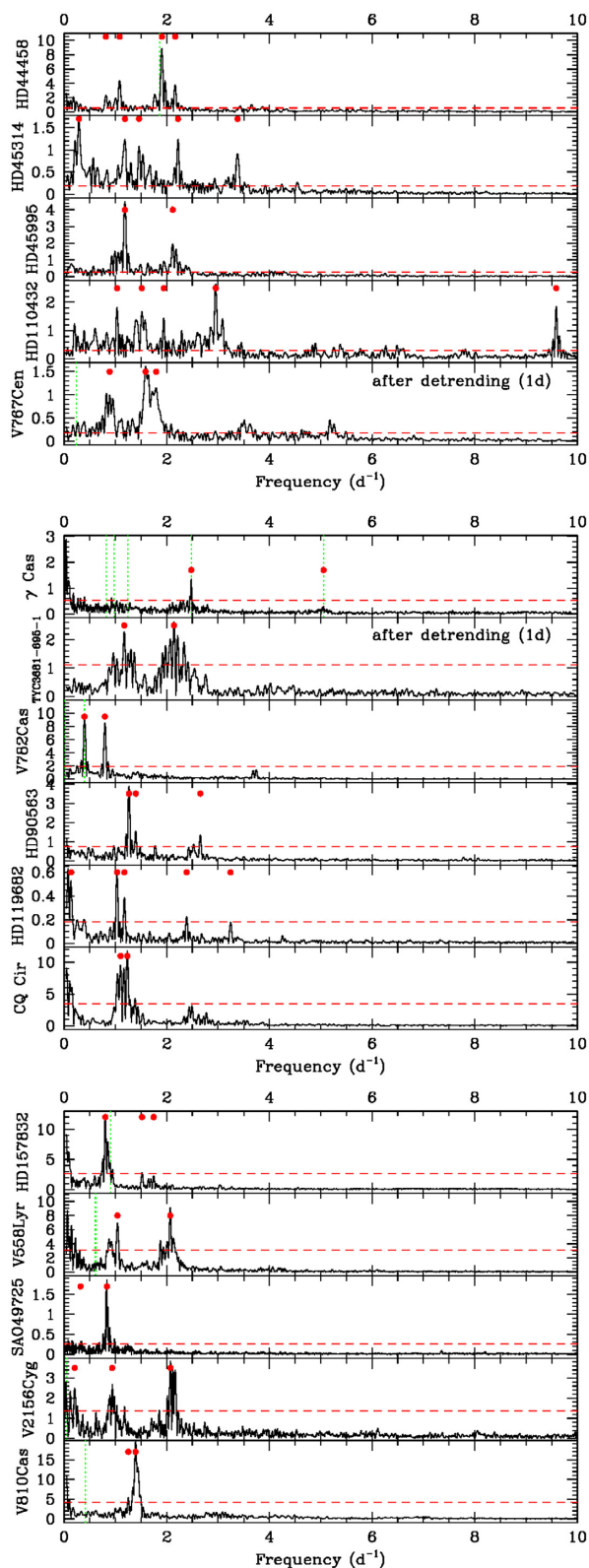


**Figure 2.** Fourier periodograms associated to the light curves shown in Fig. 1; the ordinate provides sinusoid amplitudes in mmag. For TYC 3681-695-1 and V767 Cen, only the periodograms of the detrended light curve are presented. The dashed red horizontal line provides the 1 per cent significance level while dotted green vertical lines show the frequencies of previously reported signals and small red dots indicate the frequencies which were whitened to search for specific variability (see Section 2).

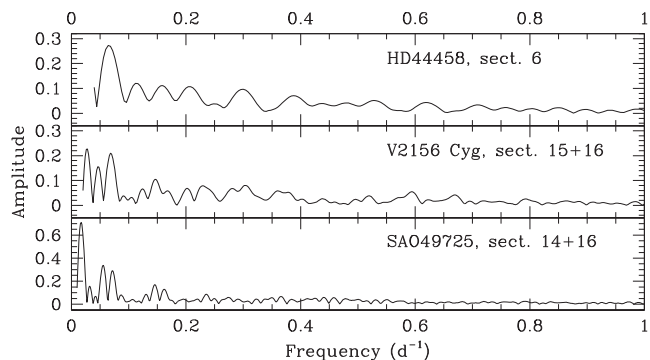


**Figure 3.** Spectral windows derived for one or two sectors, showing expected aliases.

significance level derived using the formula of Mahy et al. (2011).<sup>3</sup> In addition, to assess the evolution of the variability, we derived the periodograms in sliding windows of 5 d duration shifted by steps of 0.5 d. Finally, to search for faint signals (especially at high frequencies) and for red noise, we subtracted the strongest signals. This was done by first detrending the data using a 5 d sliding window (except for TYC 3681-695-1 and V767 Cen, for which detrending was already done before) and then taking out the 2–5 sinusoids corresponding to the strongest peaks (Fig. 2).

### 3 RESULTS

#### 3.1 Types of variability

While there are no two identical periodograms, some general features can be identified in Fig. 2. First, the power mostly lies at low frequencies, usually below  $3 \text{ d}^{-1}$ . Secondly, signals either appear as rather isolated peaks or form broad frequency groups. Those groups are genuine features, not just a peak and its close aliases, although faint aliases (due to holes in sampling) can of course also be detected (see also spectral windows in Fig. 3).

To further detail the observed variability, we subdivide the periodogram features into four different types (see next). To summarize our results, Table 1 gathers the properties of all stars, listing the significant signals and their properties.

(i) *Long-term variations*: Be stars are known to vary on long time-scales but *TESS* photometric data only cover 1 month per sector, so can only provide a glimpse of the long-term properties of  $\gamma$  Cas stars. In our data set, large and slow changes are seen in only two stars: TYC 3681-695-1 and V767 Cen. The amplitude of these photometric changes are 0.1–0.3 mag, comparable to what was observed for  $\pi$  Aqr and HD 110432 in Nazé et al. (2020b). Shallower long-term trends ( $<0.04$  mag), resulting in some signal appearing at the lowest frequencies in the periodograms, are seen in nine other stars (see Table 1 for details) but they may be (at least partly) instrumental.

(ii) *Red noise*: A gradual increase in periodogram amplitudes can be seen towards the lowest frequencies, especially in HD 45314, once the light curve has been detrended and cleaned from its main periods. This so-called ‘red noise’ actually is stellar in origin, rather than instrumental, as its presence has been reported in several massive

<sup>3</sup>Formally, there exists no analytical formula to estimate the significance level of a periodogram peak in case of uneven samplings. However, the *TESS* light curves mostly consist of evenly sampled data, with only a few gaps, and the Mahy et al. formula provides a very good approximation in this case.

**Table 1.** Properties of  $\gamma$  Cas stars, as observed by *TESS*, ordered by RA; the list of previously reported frequencies (see Section 3.3) is also added for completeness.

| Name                  | Star | Alt. name | Spectral Type   | V (mag) | <i>TESS</i> sector(s) | LTV (mmag) | FG ( $d^{-1}$ ) | Coherent frequencies ( $d^{-1}$ ) (<5 $d^{-1}$ ) | Coherent frequencies ( $d^{-1}$ ) (>5 $d^{-1}$ ) | Literature $f$ ( $d^{-1}$ )     |
|-----------------------|------|-----------|-----------------|---------|-----------------------|------------|-----------------|--|--|---------------------------------|
| $\gamma$ Cas          |      |           |                 |         |                       |            |                 |  |  |                                 |
| TYC 3681-695-1        |      | HD 5394   | B0 IVpe         | 2.39    | 17,18                 | 10         | 1.2,3.5         | 2.480(D)   | 5.054,7.572                                      | 0.822, 0.97, 1.246, 2.479, 5.06 |
| V782 Cas              |      | ALS 6507  | B1-2 III/Ve     | 11.36   | 18                    | 110        | 1.2,2.1         | —  | —  | —                               |
| HD 44458 <sup>a</sup> |      | HD 12882  | B2.5 III:In]e + | 7.62    | 18                    | <6         | —               | 0.396(D),0.796,1.424,3.684,3.744                 | —  | 0.021, 0.398                    |
| HD 45314 <sup>a</sup> |      | FR CMa    | B1 Vpe          | 5.55    | 6                     | 10         | 0.9,1.9         | 0.816(c),1.084,1.904,2.164                       | —  | 1.866                           |
| HD 45995 <sup>a</sup> |      | PZ Gem    | O9pe            | 6.64    | 6                     | <2         | —               | 0.288(c),1.184,1.460,2.220,3.380                 | 18.080   | —                               |
| HD 90563              |      | ALS 8975  | B2 Vnne         | 6.14    | 6                     | <2         | 1.1,2.1         | 1.184(D)   | 6.256  | —                               |
| HD 119682             |      | ALS 1556  | B2 Ve           | 9.86    | 10                    | 3          | 2.5,8,10.6      | 1.264(D),1.396(c),1.776,2.656                    | —  | —                               |
| V767 Cen <sup>a</sup> |      | ALS 3157  | B0 Ve           | 7.90    | 11                    | 1.5        | —               | 0.140(c),1.032,1.176,2.388,3.244                 | —  | —                               |
| CQ Cir                |      | HD 120991 | B2 Ve           | 6.10    | 11                    | 300        | 0.9,1.7,3.5,5.2 | —  | 6.812  | 0.23474                         |
| HD 157832             |      | HD 130437 | B1 Ve           | 10.04   | 11                    | 20         | 1.2,2.5         | —  | —  | —                               |
| V558 Lyr              |      | V750 Ara  | B2 Vne          | 6.66    | 12                    | 25         | 0.8,1.7         | 0.804(D),1.520                                   | —  | 0.906                           |
| SAO 49725             |      | HD 183362 | B3 Ve           | 6.34    | 14                    | 35         | 0.9,2.0         | 1.040,2.068                                      | —  | 0.60972, 0.62625                |
| V2156 Cyg             |      | ALS 11396 | B0.5 III-Ve     | 9.27    | 14,16                 | <3         | —               | 0.833(D)   | 7.359,8.194(c)                                   | —                               |
| V810 Cas              |      | HD 220058 | B1 npe          | 8.91    | 15,16                 | 15         | 0.2,0.9,2.1     | —  | —  | 0.048                           |
|                       |      |           |                 | 8.59    | 17                    | 15         | —               | 1.252,1.392(D)                                   | —  | 0.418                           |

<sup>a</sup> indicates observations taken with 2 min cadence, (D) dominant frequencies, and (c) peak possibly arising from signal combination. Spectral types are taken from Smith et al. (2016), Nazé & Moich (2018), and Nazé et al. (2020b), while V magnitudes are from Simbad. LTV corresponds to ‘long-term variations’ and their amplitudes were estimated from the trend determined using a sliding average (see Section 2 for details). FG stands for ‘frequency groups’: because of their broadness, their frequency is approximate and therefore provided with only one decimal. For coherent signals listed in the next two columns, it should be noted that the typical peak widths in periodograms are 0.04  $d^{-1}$  for observations in one sector or less for multisector cases (0.02  $d^{-1}$  for  $\gamma$  Cas and V2156 Cyg, 0.01  $d^{-1}$  for SAO 49725); the errors on the peak frequencies will be a fraction of that value (typically one tenth).

stars (Blomme et al. 2011; Bowman et al. 2019; Rauw et al. 2019). Subsection 3.1.1 provides further details on the properties of the red noise in our targets.

(iii) *Frequency groups*: Rather than isolated peaks, some periodograms show broad groups. In our sample, these frequency groups are dominating the periodograms of TYC 3681-695-1, V767 Cen, CQ Cir, and V2156 Cyg. Except for CQ Cir, two main groups are present in each star, with the one at a higher frequency having a larger amplitude than the one at a lower frequency. In other stars (especially HD 45995 and V558 Lyr, but see details in Table 1), a strong peak may be accompanied by a dense set of neighbouring fainter peaks, pointing to the presence of a low-amplitude frequency group.

(iv) *Coherent signals*: When a peak appears strong, isolated, and with a relatively stable frequency (throughout our observations, see Section 3.2, and/or comparing with other data sets, see Section 3.3), the signal may be assumed to be coherent. Table 1 lists the candidate frequencies. Many stars in our sample appear to possess such signals, with various properties: some peaks are dominant (see next) while others are not; most are at low frequencies while a few others, with low amplitudes, appear at high frequencies (see further details in Section 3.1.2); some are in harmonic ratio (see Appendix) while others could be combinations of signals; some appear clearly separated from frequency groups while others appear on top of frequency groups (but clearly dominating them).

(a) *Dominant signal*: Some periodograms show a single peak, without any other frequency or with only much fainter other signals. In our sample, this is particularly the case of SAO 49725 and V810 Cas, whose periodograms present a single peak. The periodograms of five other stars are dominated by one frequency (with its strong harmonics for V782 Cas), but fainter signals at different frequencies are also present. In some cases (especially HD 45995, HD 157832, SAO 49725, and V810 Cas), prewhitening the light curves by these dominant frequencies still leaves significant residuals. This could be an effect of the evolving variability (see Section 3.3) or reflect the complexity of the underlying signal (actually not a single, pure frequency).

### 3.1.1 Red noise

To assess the presence of red noise in the sample of  $\gamma$  Cas stars, we adopt the formalism of Stanishchev et al. (2002) to fit the periodogram with an expression:

$$A(\nu) = \frac{A_0}{1 + (2\pi\tau\nu)^\gamma} + C, \quad (1)$$

where  $A_0$  is the red noise level at nul frequency,  $\tau$  the mean lifetime of the structures producing the red noise,  $\gamma$  the slope of the linear decrease, and  $C$  the white noise level.

The parameters of this relation were determined from a fit to the periodogram detrended and prewhitened for the most prominent frequencies (see Fig. 4 for examples). For most stars, the fit of the red noise parameters was performed over the frequency range from 0.1 to 10  $\text{d}^{-1}$ , and the level of white noise  $C$  was determined from the periodogram mean between 12 and 25  $\text{d}^{-1}$ , where red noise is negligible. However, in a few cases, the red noise extended to higher frequencies and we thus performed the fit of the red noise up to 15  $\text{d}^{-1}$ , and in one case to 20  $\text{d}^{-1}$ . In those cases, the white noise level was determined from the mean between 20 and 25  $\text{d}^{-1}$ .

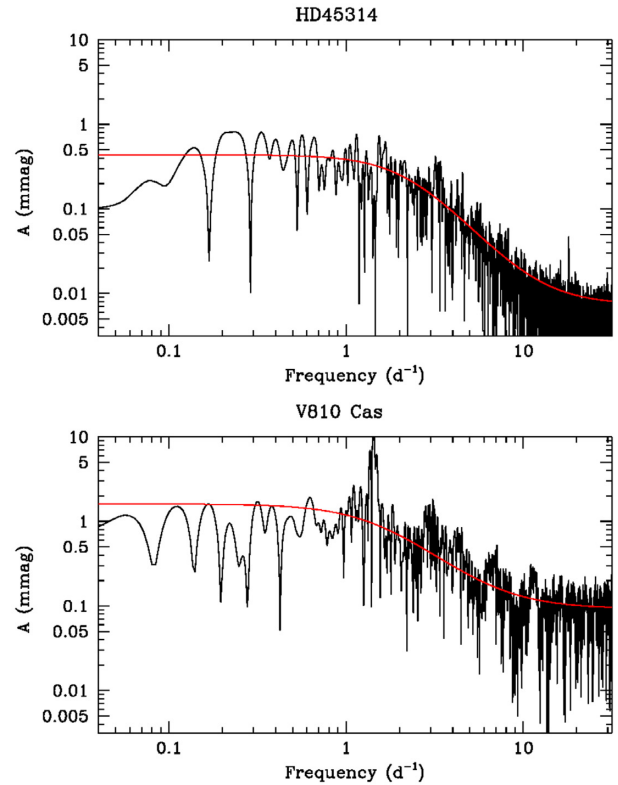


**Figure 4.** Log–log plots of the periodograms of the detrended and prewhitened *TESS* photometry of HD 45314 and V810 Cas. The red curves correspond to the red-noise relations described by parameters from Table 2.

**Table 2.** White noise and red noise parameters in *TESS* data of  $\gamma$  Cas stars, ordered by RA.

| Star                  | $A_0$<br>(mmag) | $\gamma$        | $\tau$<br>(d)     | $C$<br>(mmag) |
|-----------------------|-----------------|-----------------|-------------------|---------------|
| $\gamma$ Cas          | $0.31 \pm 0.09$ | $1.82 \pm 0.73$ | $0.139 \pm 0.080$ | 0.025         |
| V782 Cas              | $0.63 \pm 0.19$ | $1.73 \pm 0.69$ | $0.152 \pm 0.098$ | 0.016         |
| HD 44458 <sup>a</sup> | $0.47 \pm 0.07$ | $2.34 \pm 0.59$ | $0.051 \pm 0.013$ | 0.013         |
| HD 45314              | $0.43 \pm 0.04$ | $2.44 \pm 0.42$ | $0.070 \pm 0.010$ | 0.007         |
| HD 90563 <sup>a</sup> | $0.32 \pm 0.09$ | $1.76 \pm 0.71$ | $0.105 \pm 0.059$ | 0.019         |
| HD 119682             | $0.11 \pm 0.04$ | $1.67 \pm 0.67$ | $0.281 \pm 0.163$ | 0.005         |
| V558 Lyr              | $1.41 \pm 0.38$ | $1.99 \pm 0.78$ | $0.100 \pm 0.053$ | 0.032         |
| V810 Cas              | $1.52 \pm 0.29$ | $2.03 \pm 0.77$ | $0.099 \pm 0.051$ | 0.093         |

<sup>a</sup>Fit performed over the frequency range 0.1–15  $\text{d}^{-1}$ .

Some remarks must be made on this procedure. First, no fit could be obtained for TYC 3681-695-1 as significant red noise seems undetectable in the periodogram of this star. Second, the prewhitening was imperfect in some cases, especially when complex variability (frequency groups) was present. In those cases, lots of residual signals remain at low frequencies, which bias the red noise estimates. Therefore, the fitting certainly overestimates the red noise for HD 45995, CQ Cir, and V2156 Cyg (for which the fit was moreover of poor quality) and it somewhat overestimates it for HD 110432, V767 Cen, HD 157832, and SAO 49725. For all those stars, the actual red noise parameters remain uncertain. Only the parameters fitted to the remaining cases, for which good and reliable fits could be achieved, are presented in Table 2. It is important to note that these values are fully compatible with those observed for massive OB stars (Bowman et al. 2020).

### 3.1.2 Presence of high-frequency signals

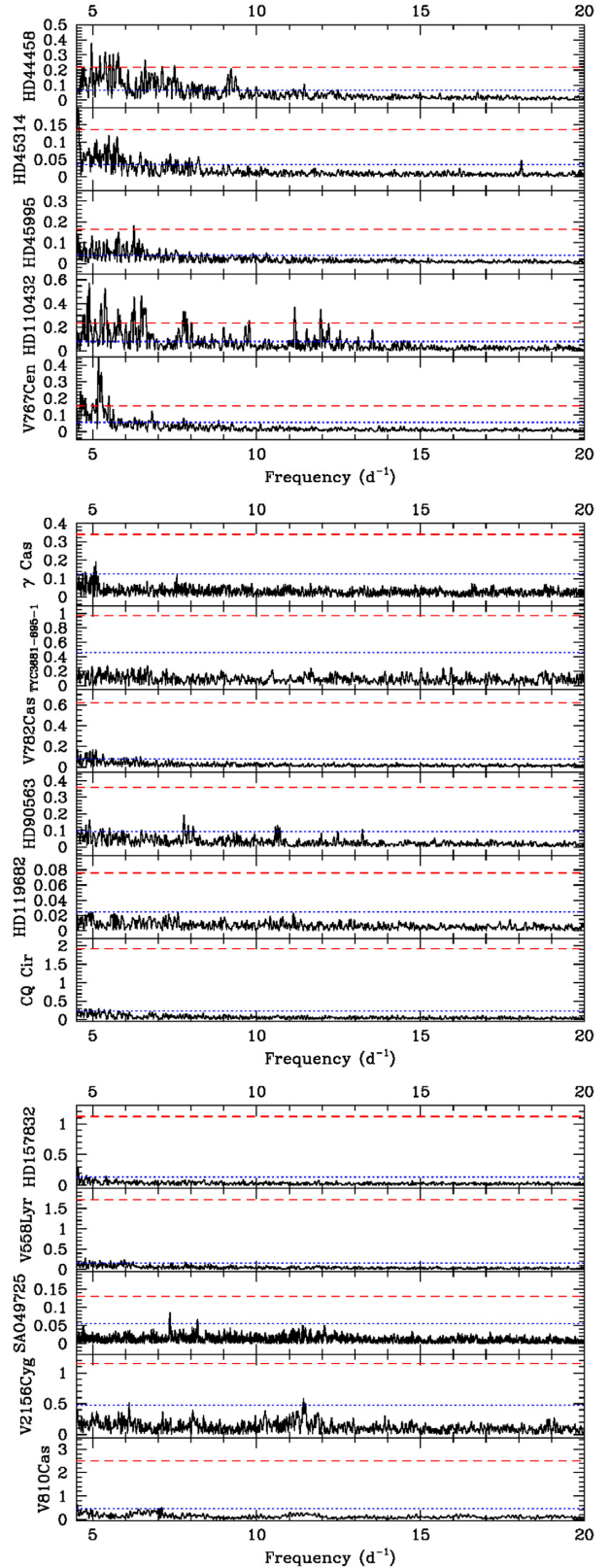
All stars studied in this paper display clear variability at low frequencies but are they also varying at high frequencies? In Nazé et al. (2020b), the two  $\gamma$  Cas analogues  $\pi$  Aqr and HD 110432 were found to display coherent high-frequency variations ( $f > 5 \text{ d}^{-1}$ ) with amplitudes of  $\sim 1 \text{ mmag}$ . In the *SMEI* data of  $\pi$  Aqr, the 2–12  $\text{d}^{-1}$  periodogram was in fact dominated by high-frequency signals (appearing at 7.3, 8.3, 11.6, 11.8  $\text{d}^{-1}$ ). In the *TESS* data of HD 110432 (Fig. 2 and Nazé et al. 2020b), the high-frequency signal at 9.588  $\text{d}^{-1}$  appears as strong as the low-frequency ones, and there are also numerous faint signals at 4.5–7  $\text{d}^{-1}$ , near 7.8 and 11.956  $\text{d}^{-1}$ , as well as isolated signals at 11.164 and 13.528  $\text{d}^{-1}$ .

At first sight, nothing similar can be found in the 15 *TESS* light curves analysed here (Fig. 2). However, low-level signals may be present but be difficult to detect when other signals dominate. The *TESS* light curves were therefore detrended and prewhitened for the strongest signals to search for them (Section 2, Fig. 5). Since the 1 per cent significance level derived using the Mahy et al. (2011) formula considers the full light curve scatter, whatever the variability frequency, it underestimates the significance of high-frequency signals when red noise is present or in case of imperfect cleaning at low frequencies (in other words, whenever there remain low-frequency signals). Therefore, we used as an alternative for detection five times the white noise level determined in Section 3.1.1 (see Fig. 5).

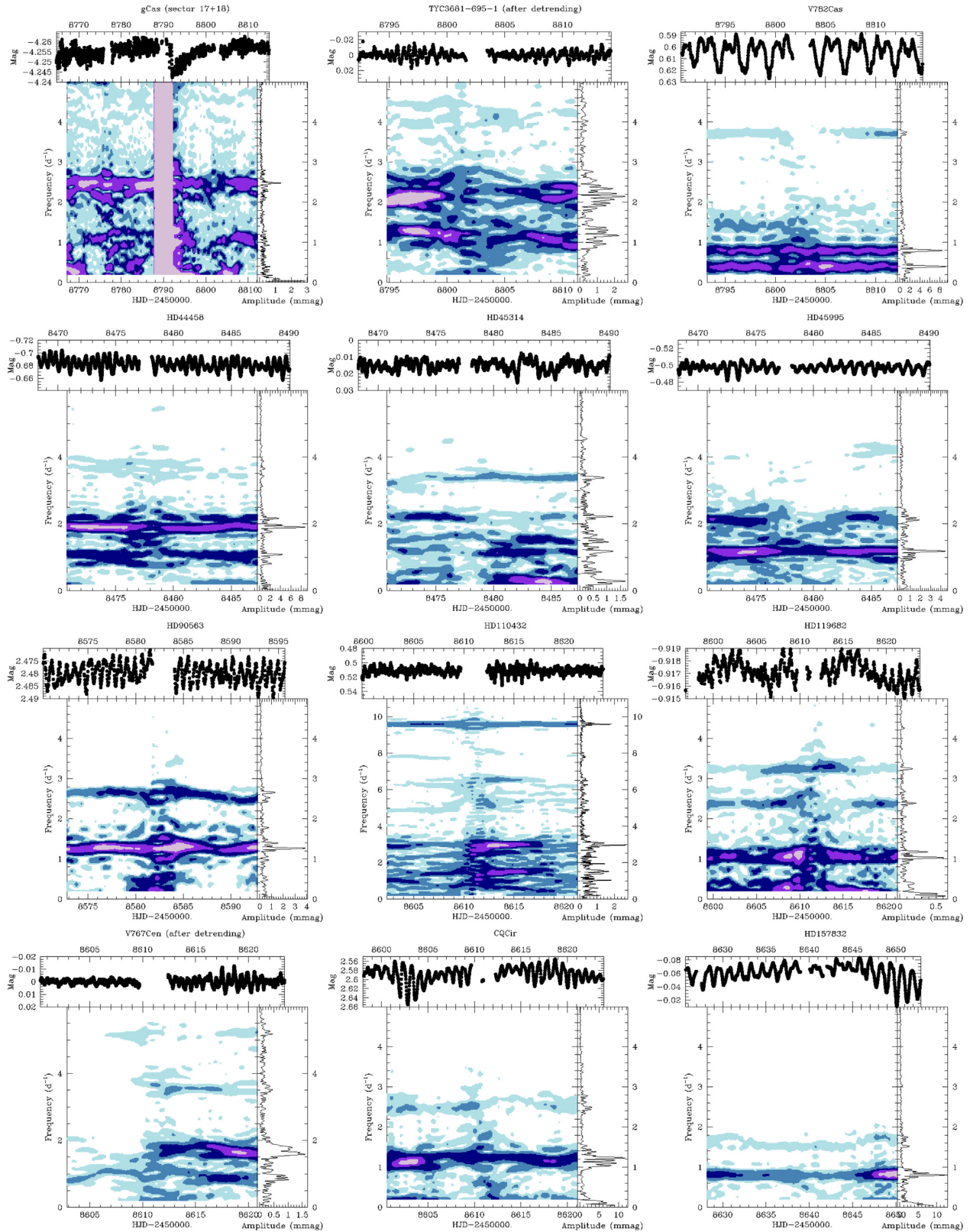
HD 44458 presents many low-level signals up to 10  $\text{d}^{-1}$ , without clearly isolated peaks (which could be groups or red noise). HD 45314 displays an isolated peak at 18.080  $\text{d}^{-1}$ , while for HD 45995, a significant and rather isolated peak is present at 6.256  $\text{d}^{-1}$ . V767 Cen displays a significant frequency group near 5.2  $\text{d}^{-1}$ , plus an isolated peak at 6.812  $\text{d}^{-1}$ . The periodogram of  $\gamma$  Cas shows a peak at 5.054  $\text{d}^{-1}$ , which is accompanied by another, even fainter one at 7.572  $\text{d}^{-1}$  (it barely reaches significance). The periodogram of HD 90563 has small frequency groups near 8 and 10.6  $\text{d}^{-1}$  while SAO 49725 shows isolated peaks at 7.359 and 8.194  $\text{d}^{-1}$ . All these signals reach amplitudes of 0.05–0.4 mmag, i.e. much less than for HD 110432 or  $\pi$  Aqr: clearly, our targets do not display strong high-frequency signals but half of them (7 of 15 if considering groups) display low-level ones.

### 3.2 Temporal evolution

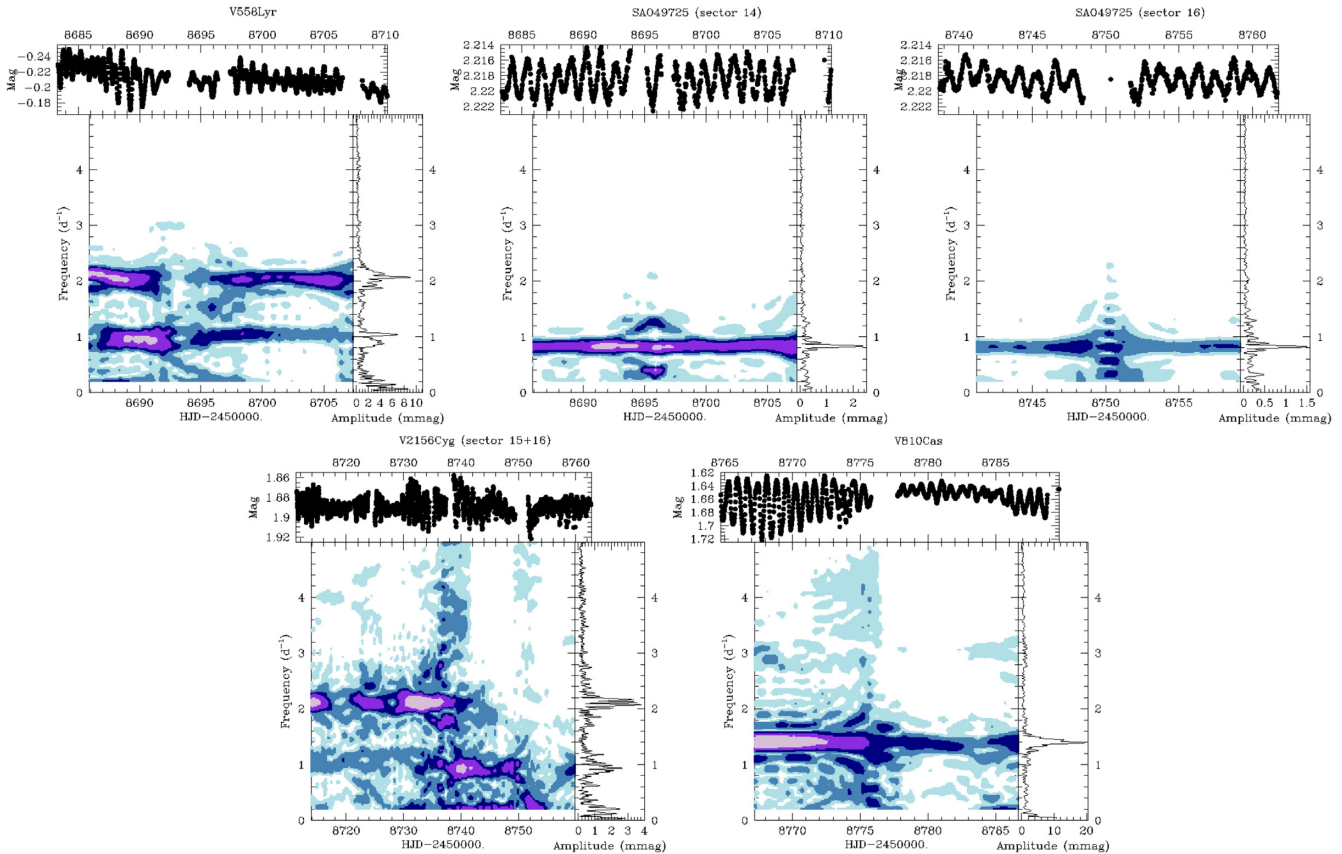
As mentioned at the end of Section 2, we also derived periodograms in sliding windows of 5 d duration shifted by steps of 0.5 d. These time–frequency diagrams (Fig. 6) enable to study the temporal evolution of the detected signals, although with a reduced frequency resolution (whatever the frequency, the natural peak widths are 0.04  $\text{d}^{-1}$  for the full data set of one sector, or 0.01–0.02  $\text{d}^{-1}$  for multisector cases, but only 0.2  $\text{d}^{-1}$  here). Only the periodograms of V782 Cas, HD 44458, HD 45995, HD 90563, and HD 119682 appear relatively stable. Rather large changes are seen in all other cases, with two main categories. In the first category, the same frequencies (at the resolution limit) seem to be always present in the periodograms, but with changing amplitudes – varying oscillation amplitudes can also be spotted in light curves. This occurs in  $\gamma$  Cas, HD 157832, V558 Lyr, SAO 49725, and V810 Cas, as well as in HD 110432 (especially for their main signals). Changes can be very localized (as for example in HD 157832) or occurs more slowly. For example, the variations of SAO 49725 were stronger in the first observing window (sector 14) than in the second one (sector 16) but the amplitude remains rather stable within a given window. An intermediate case



**Figure 5.** Fourier periodograms at high frequencies, after detrending and prewhitening the *TESS* light curves (see Section 2); the ordinate provides sinusoid amplitudes in mmag. In each panel, the dashed red horizontal line provides the 1 per cent significance level using the formula of Mahy et al. (2011), whereas the dotted blue horizontal line yields five times the white noise level (see text for details).



**Figure 6.** Time–frequency diagrams for all targets; the dates in abscissa correspond to the mid-point of the temporal window used for calculating the periodogram. The light curve is displayed on top, whilst the periodogram for the full data set is shown on the right. For the stars with multisector information, the same amplitudes are used for the colour levels, to spot changes more easily. For the two stars with strong long-term changes, only the analysis of the detrended light curve is provided.

Figure 6 – *Continued*

is V810 Cas, with its amplitude strengthening covering one half of a sector. In TYC 3681-695-1 and CQ Cir, the frequency groups also seem to be always present (with varying details, though). A second set of light curves display changes in both the frequency content and the amplitude of the signals. This seems to be the case for HD 45314 (especially at low frequencies), V767 Cen, and V2156 Cyg. For the latter star, the signal near  $2 \text{ d}^{-1}$  clearly dominates during the first observing season (sector 15), whereas the second one (sector 16) rather shows low frequencies and signals near  $1 \text{ d}^{-1}$ .

In this context, it is interesting to search for links between the short- and long-term variabilities. For V767 Cen, the short-term oscillations appear maximum towards the end of the observing window, more precisely at the maximum of a shallow brightness ‘bump’ which itself follows a phase of slow decay. For this star, it does not seem that strong oscillations are triggering an outburst leading to a luminosity increase (as e.g. proposed for HD 49330, Huat et al. 2009). In parallel, the short-term variations of TYC 3681-695-1 have a larger amplitude during a brightness maximum but also during a luminosity increase occurring at the end of the observing window.

### 3.3 Variability in other data sets

The photometric variability of our targets has been previously studied, except for TYC 3681-695-1, HD 90563, HD 119682, and SAO 49725. In three other cases, the published information is very limited: HD 45995 was reported in the *Hipparcos* catalogue as photometrically variable, more precisely it had ‘duplicitly-induced variability’ (see also Olsen 1982); HD 45314 and CQ Cir were reported as photometrically variable in the *Hipparcos* catalogue

and by Lefèvre et al. (2009). No periodic signal was previously mentioned in the literature for those three stars, however. This work thus presents the first detailed photometric study for these targets. For the remaining stars, more information exists and it is mentioned in the dedicated items below, along with a comparison to our findings. To further facilitate this comparison, the last column of Table 1 lists the previously reported frequencies (also shown in Fig. 2 as the vertical green lines), while Fig. 7 compares *TESS* periodograms with those derived from published high-quality data sets from *Kepler* and *KELT* (Labadie-Bartz et al. 2017; Pope et al. 2019).

In parallel, we searched for additional data of our targets in several extensive photometric data bases: *SuperWASP*<sup>4</sup> (Butters et al. 2010), *ASAS*<sup>5</sup> (Pojmanski 1997), and *ASAS-SN*<sup>6</sup> (Shappee et al. 2014). For *SuperWASP*, as done for *TESS*, the data points with errors larger than the mean of the errors plus their  $1\sigma$  dispersion were discarded. The derived periodograms are compared to the *TESS* ones in Fig. 7. For the latter two surveys, outliers and bad quality data were excluded but the noise often remained too large for detecting the subtle signals found in *TESS* photometry. Therefore, Fig. 7 only presents the favorable cases. A short (8 d) high-cadence *BRITE*<sup>7</sup> (Weiss et al. 2014) run was available for V767 Cen and is here added for completeness, although it does not reveal any clear signal (Fig. 7).

<sup>4</sup><https://exoplanetarchive.ipac.caltech.edu/cgi-bin/TblSearch/nph-tblSearchInit?app=ExoTbls&config=superwasptimeseries>

<sup>5</sup><http://www.astrouw.edu.pl/asas/?page=aasc>

<sup>6</sup><https://ASAS-SN.osu.edu/>

<sup>7</sup><http://brite.camk.edu.pl/pub/index.html>

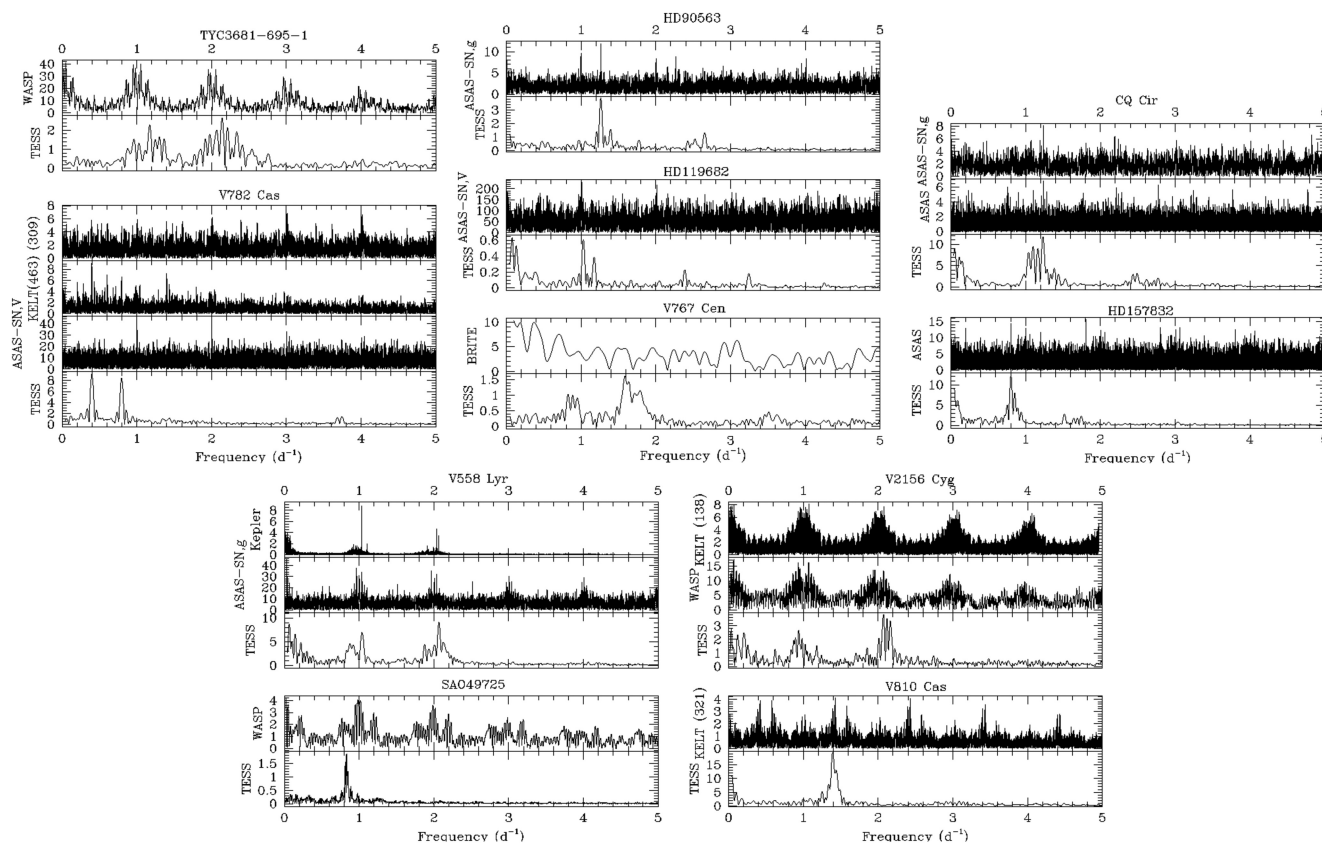


**Figure 7.** Comparison between periodograms derived for four stars from *TESS* and other observations; the ordinate provides sinusoid amplitudes in mmag. For *KELT*, the identification numbers from Labadie-Bartz et al. (2017) are quoted between parentheses.

Notes on individual stars:

(i)  $\gamma$  Cas has been the target of many studies, including several on its photometric short-term optical variability. Using 15 seasons of ground-based APT data, Smith, Henry & Vishniac (2006) and Henry & Smith (2012) detected a frequency of  $0.82 \text{ d}^{-1}$  with variable amplitude. The signal appeared lower in 2004–2011 compared to 1997–2003. Borre et al. (2020) confirmed these results using *SMEI* space-based data taken over the same years. In recent *BRITe* space-based observations, the strength of this signal seems to have further faded, becoming undetectable. The dominant frequency now seems to be a signal at  $2.48 \text{ d}^{-1}$  frequency (Borre et al. 2020). The same authors also reported an additional signal at  $1.25 \text{ d}^{-1}$  as well as potential detections near  $0.97$  and  $5.06 \text{ d}^{-1}$ . In the *TESS* data, the main signal clearly is  $2.48 \text{ d}^{-1}$  and a peak at  $5.054 \text{ d}^{-1}$  also seems to be present. There is, however, no trace of the signals at  $0.82$ ,  $0.97$ , and  $1.25 \text{ d}^{-1}$  – there are many small peaks in this region. Meanwhile, APT observations from the most recent seasons confirm the presence of the  $2.48$  and  $5.06 \text{ d}^{-1}$  signals; no other frequencies are visible in those data (Smith and Henry, in preparation).

(ii) TYC 3681-695-1 was also observed by *SuperWASP* (Fig. 7). While some signal is detected in the periodogram, there are a strong daily aliasing and much larger amplitudes than in *TESS*. The agreement with the frequency groups detected by *TESS* near  $1$  and  $2 \text{ d}^{-1}$  is thus difficult to ascertain.

(iii) V782 Cas was reported as ‘unsolved variable’ in the *Hipparcos* catalogue and in Nichols et al. (2010). Using *Hipparcos* data, Lefèvre et al. (2009) derived a period of  $47.621 \text{ d}$  and attributed an  $\alpha$  Cyg nature to the star. The *TESS* light curve only covers

$25 \text{ d}$ : this is more than half a  $47.621 \text{ d}$  cycle and variations due to this cycle should thus be readily seen. However, no significant long-term modulation seems present for this star. More recently, *KELT* data indicated a period of  $2.5131700 \text{ d}$  (Labadie-Bartz et al. 2017), which we confirm in *TESS* data and possibly in *ASAS-SN* observations (Fig. 7). These variations (Fig. 1) present a strong similarity with eclipses, hence we further examine this possibility in the Appendix.

(iv) HD 44458 had been found to display quite large dispersions of its *V* magnitude and *U* – *B* colours in Feinstein & Marraco (1979) and was reported as ‘unsolved variable’ in the *Hipparcos* catalogue. Using *Hipparcos* data, Hubert & Floquet (1998) derived a period of  $0.536 \text{ d}$  which was confirmed by Percy et al. (2002) using autocorrelation methods. This period is close to the strongest signal in the *TESS* periodogram.

(v) HD 90563 display the same main signal in *TESS* and *ASAS-SN* data, though with a different amplitude (Fig. 7).

(vi) HD 119682 has some signal in its *ASAS-SN* periodogram near the *TESS* detection, but close to the daily alias and with a much larger amplitude, casting some doubt on the *ASAS-SN* detection.

(vii) V767 Cen has long been known to be variable, notably showing quite large dispersions of its *V* magnitude and *B* – *V*, *U* – *B* colour measurements (Corben 1966; Feinstein 1975; Feinstein & Marraco 1979). The presence of changes was confirmed by Dachs & Lemmer (1989), Dougherty & Taylor (1994), Moujtahid et al. (1998), and the *Hipparcos* data (the star appears as ‘unsolved variable’ in the catalogue). Further analysis of the *Hipparcos* data indicated outbursts recurring with a time-scale of about  $300 \text{ d}$  (Hubert & Floquet 1998) and a periodicity with  $f = 0.23474 \text{ d}^{-1}$  (Koen & Eyer 2002). The

*TESS* light curve indicates long-term variability, which could be in line with the recurrent outbursts, but shows no sign of the proposed period (Fig. 2).

(viii) CQ Cir shows hints of the principal peak in the main frequency group detected by *TESS* in both *ASAS* and *ASAS-SN* data, though with varying amplitudes (Fig. 7).

(ix) HD 157832 has been found to be variable long ago (Cousins 1973; Stagg 1987). It appears with a period of  $1.10406 \pm 0.00006$  d in the *Hipparcos* catalogue, which was confirmed by Hubert & Floquet (1998), Percy, Harlow & Wu (2004), and Dubath et al. (2011). In the *TESS* data, the main period appears close but significantly longer than this value. However, with their overall scarcity, leading to strong aliasing, the *Hipparcos* data are not adapted for clear detections of such high frequencies. Besides, the peak in the *TESS* periodogram appears somewhat broad, with a submaximum corresponding to the *Hipparcos* value (Fig. 2). Finally, it may be noted that the *ASAS* data also confirm the *TESS* results (Fig. 7).

(x) V558 Lyr was reported as ‘unsolved variable’ in the *Hipparcos* catalogue. Molenda-Zakowicz & Polubek (2005) detected two frequencies, 0.60972 and 0.62625  $\text{d}^{-1}$ , in *Hipparcos* photometry. More recently, Pope et al. (2019) found ‘hump and spike’ features near 1 and 2  $\text{d}^{-1}$  in *Kepler* data, without any signal near 0.6  $\text{d}^{-1}$  (see their fig. 11). We also fail to detect signals near 0.6  $\text{d}^{-1}$  but *TESS* observations, and possibly *ASAS-SN* data, confirm the *Kepler* signals (Fig. 7).

(xi) SAO 49725 seems to display frequency groups in the *SuperWASP* periodogram, in particular signal exists at similar frequencies as in *TESS* data, but there is not a dominant central peak.

(xii) V2156 Cyg, reported as ‘unsolved variable’ in the *Hipparcos* catalogue, was found to have a period of 21.0346600 d in *KELT* data (Labadie-Bartz et al. 2017), without outbursts (Labadie-Bartz et al. 2018). The star was observed in two consecutive sectors by *TESS*, hence the data cover more than 50 d. While there is no obvious trace of a 21 d cycle in the *TESS* light curve, the periodogram indicates the presence of a low-frequency signal, especially during the second observing window. However, its value is only marginally compatible with the *KELT* detection (strongest *TESS* peak is at  $28 \pm 3$  d in the combined periodogram). Fig. 7 directly compares the *KELT*, *SuperWASP*, and *TESS* periodograms: the presence of a strong daily alias renders the identification of the frequency groups detected by *TESS* more difficult in the former two cases, but there seems to be an agreement between data sets.

(xiii) V810 Cas, reported as ‘unsolved variable’ in the *Hipparcos* catalogue, displays slow variations according to Lefèvre et al. (2009) but *KELT* data rather indicated a rather short periodicity (2.3904100 d, Labadie-Bartz et al. 2017). The *TESS* data reveal an even shorter period, of which the *KELT* detection is a daily alias: the absence of *TESS* signal at the *KELT* frequency and the strong daily aliasing in *KELT* periodograms are shown in Fig. 7.

## 4 DISCUSSION

In the previous section, we presented the analysis of the *TESS* data of 15  $\gamma$  Cas analogues. The targets display isolated frequencies or a few frequency groups, sometimes in harmonic relation and always appearing at low frequencies ( $f < 5 \text{ d}^{-1}$  – only a few faint high-frequency signals are detected). The high-cadence, space-borne photometry of three  $\gamma$  Cas stars had already been studied ( $\gamma$  Cas, Borre et al. 2020; HD 110432 and  $\pi$  Aqr, Nazé et al. 2020b), as well as the high-quality photometric data sets of several ‘normal’ (i.e. non- $\gamma$  Cas) Be stars (e.g. Labadie-Bartz et al. 2017; Semaan et al. 2018; Balona & Ozuyar 2020), allowing for a global comparison.

First, the global appearance of periodograms can be compared. Analyzing 57 Be stars observed by *TESS*, Balona & Ozuyar (2020) reported that 40 per cent of the stars displayed a simple periodogram (one peak or two peaks in harmonic relation with little broadening or only some fine structure), while 30 per cent were more complex (frequency group or groups in harmonic relation). Amongst the 15 Be stars observed by *CoRoT* (Semaan et al. 2018), about 30 per cent displayed strong frequency groups while a fifth of the sample had only a single peak dominating their periodogram. In the sample studied here, complemented by the previously studied cases of  $\pi$  Aqr and HD 110432 (Nazé et al. 2020b), we found that  $\sim 40$  per cent of the stars display a relatively simple periodogram (i.e. with a dominant frequency) while a quarter shows strong frequency groups. Therefore, our  $\gamma$  Cas sample and the Be samples appear to be similar, especially considering the uncertainties due to small number statistics. Note that the separation between the two extreme cases mentioned here (single narrow versus broad groups) does not appear clear cut, as intermediate cases (relatively strong peaks over fainter broad groups) are often seen in our sample.

With the advent of high-precision space-borne photometry, it has also been found that a number of massive OB stars display elevated signal levels at low frequencies, aka ‘red noise’, in their photometric times series (e.g. Blomme et al. 2011; Ramiaramantsoa et al. 2018; Rauw et al. 2019; Bowman et al. 2019, 2020). Our  $\gamma$  Cas stars are no exception, showing that these stars fit the typical behaviour seen for stars of similar spectral types. The most popular scenarios to explain red noise variability are unresolved randomly excited internal gravity waves generated either in a subsurface convection zone or at the interface between the convective core and the radiative envelope (see Aerts & Rogers 2015; Ramiaramantsoa et al. 2018; Bowman et al. 2019, 2020, and references therein). Concerning the latter, Rogers et al. (2013) showed that such internal gravity waves could transport significant amount of angular momentum to the stellar surface and thereby play a key role in the formation of Be decretion discs.

The most frequent periods reported by Labadie-Bartz et al. (2017) for 510 Be stars observed by *KELT* without saturation are near 0.5 and 1.5 d (i.e. frequencies near 0.7 and 2  $\text{d}^{-1}$ ), in line with our results. Similar conclusions are reached by looking at the periodograms shown by Semaan et al. (2018) and Balona & Ozuyar (2020). It may be further noted that three quarters of our 15 targets display coherent signals with  $P < 2$  d, while at least 28 per cent of early-type Be stars of the *KELT* sample do. Besides small number statistics, the lower percentages of such detections in the *KELT* sample may probably be explained: using space facilities allows for detecting fainter and higher frequency signals (because of improved sensitivity and denser sampling) compared to ground-based telescopes.

When interpreted in terms of pulsational activity, the coherent signals at low frequencies could correspond to g-modes as in slowly pulsating B (SPB) stars, while the broad frequency groups could represent dense populations of low-order g-modes (Cameron et al. 2008). In this context, the limitations of the *TESS* data sets should be taken into account. Indeed, the typical month-long observation of one sector leads to a natural peak width of  $\sim 0.04 \text{ d}^{-1}$ . Furthermore, the sampling (in particular the gap splitting the sector observations in two separate observing windows of about 2 weeks duration) creates aliases at  $f_{\text{peak}} \pm 0.06 \dots \text{d}^{-1}$  (see Fig. 3 for details). All this renders the identification of real subpeaks difficult as typical mode separations of  $0.01 \text{ d}^{-1}$  are often found, see e.g. the zooms on groups shown by Semaan et al. (2018). The presence of real flanks can however be hinted at, as prewhitening by the peak frequency often leads to remaining wings in the periodograms (aliases will on the contrary be cleaned along with the main frequency). Longer observations,

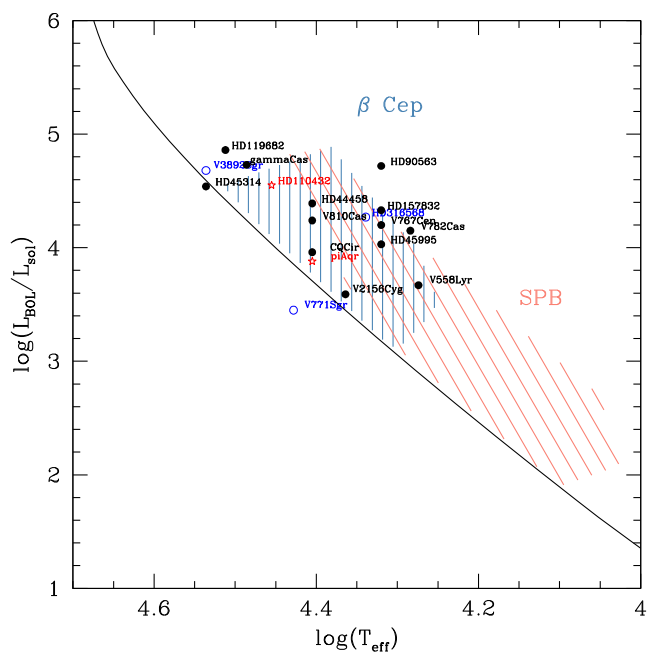
coupled to an intense spectroscopic monitoring, would certainly help confirming the presence of modes and identifying them.

Another possibility should also be considered: r-modes (Saio et al. 2018). These modes are global Rossby waves that appear in rotating stars. Because of their origin, such modes should be especially frequent in rapidly rotating stars such as Be stars (Saio et al. 2018). In a periodogram, they should form a frequency group appearing below the rotation frequency, hence their appearance of a ‘hump’ dominated by a strong peak at its high-frequency limit (explaining the ‘hump and spike’ name chosen by Saio et al. 2018). In our targets, this is clearly the case of V558 Lyr, as was already remarked by Pope et al. (2019). HD 45995 and CQ Cir could be two additional cases, but this needs to be confirmed with data taken on longer timebases, to improve the frequency resolution.

In addition to (or in place of) pulsations, rotational modulation may also arise if starspots are present on the stars. Since spots create not fully coherent variability, this could lead to frequency groups (Balona & Ozuyar 2020), allowing for an alternative interpretation of these features.

The last possibility to explain (some of) the flux variations relates to the circumstellar disc (e.g. Rivinius, Baade & Carciofi 2016). Indeed, low frequencies, close to stellar rotation, may arise from material orbiting in the inner parts of the disc. Frequency groups could then arise from circumstellar aperiodic variability superimposed on more regular features. Reprocessing of (varying) stellar illumination may also lead to apparent disc variability. Finally, in cataclysmic variables such as Z Cam, large but intermittent brightness oscillations have been recorded. They may be somewhat reminiscent of the sudden change in oscillation amplitude seen here for, e.g. V810 Cas, though with much smaller flux variations and on much shorter time-scales. Such changes are explained by a thermal-viscous instability linked to hydrogen ionisation variations in the disc (hysteresis between a bright, hot, high-viscosity state and a faint, cool, low-viscosity state, Hameury 2020). This model was extended to accretion discs in X-ray binaries and FU Ori-type stars, but it remains to be seen whether decretion discs around Be stars could also undergo a similar instability.

While low-frequency peaks, isolated or in groups, are detected, signals at higher frequencies ( $f > 5 \text{ d}^{-1}$ ) are also recorded in some stars. However, they seldom appear alone or strong, i.e. dominating the frequency content or even simply with amplitudes comparable to the low-frequency signals. In Balona & Ozuyar (2020), only  $\sim 10$  per cent of the stars displayed such strong high-frequency peaks, whereas one fifth of the 15 stars analysed by Semaan et al. (2018) do so. For  $\gamma$  Cas analogues, only two stars ( $\pi$  Aqr and HD 110432) harbour such strong signals (which makes a fraction around 10 per cent). A systematic search for signals with smaller amplitudes should certainly be undertaken, but it can already be said that half of the sample of Semaan et al. (2018) and half of our sample display peaks, faint or (relatively) strong, at these frequencies. Again, there thus seems to be a good agreement between samples. Such coherent high-frequency signals are often interpreted as p-modes and it is therefore useful to see where the targets appear in the HR diagram. When the stellar parameters from Nazé & Motch (2018) and Nazé et al. (2020a) are used, the  $\gamma$  Cas analogues are grouped in the HR diagram. Some stars appear outside the SPB locus, though they vary at low frequencies, but all appear within the  $\beta$  Cep locus (Fig. 8), hence could potentially pulsate at high frequencies.<sup>8</sup> While



campaigns such as *KELT*, which limits the possibility to observe outbursts or long-term signals.

In this context, it is important to note that the properties of the short-term oscillations do not remain constant over time, for the  $\gamma$  Cas stars as for other Be stars (Balona & Ozuyar 2020). Changes are particularly interesting to note during outbursts. The *CoRoT* cases displayed larger oscillations during outbursts (corresponding to decreasing or fading brightnesses). Generally, the amplitudes of the main frequencies increased during these events, with only fainter signals sometimes doing the contrary. In Huat et al. (2009) and Balona & Ozuyar (2020), the outbursting HD 49330 showed a decrease in the amplitude of its high-frequency signals while low-frequency groups appeared. In  $\pi$  Aqr, some high-frequency signals decreased while other increased (or appeared) during outbursts, while HD 110432 showed larger amplitudes for both low- and high-frequency signals when the star was brighter (Nazé et al. 2020b). In the two cases reported in the previous sections, an increase in oscillation amplitude was detected at the maximum of an outburst and afterwards, not before it. In the small set of stars whose oscillations were examined at and near outbursting events, there thus seems to be no general rule, as, e.g. stronger pulsations just before Be outbursts. Besides, peak changes of similar amplitudes can be noted outside outburst events (see e.g. HD 157832, V2156 Cyg, V810 Cas). Definitely, more stars should be followed in detail before drawing conclusions on the triggering effects associated to outbursts and pulsation changes.

## 5 SUMMARY AND CONCLUSIONS

This paper reports on the analysis of *TESS* light curves of 15  $\gamma$  Cas analogues, complemented by *ASAS*, *ASAS-SN*, *BRITE*, *SuperWASP* archival data. It enlarges a previous study analyzing high-cadence photometric data of two bright  $\gamma$  Cas stars. This work allows us to constrain the short-term variability properties for two thirds of the  $\gamma$  Cas sample. Studying such a significant fraction provides clear insights on the whole class.

The periodograms of these 15  $\gamma$  Cas stars present signals at low frequencies ( $f < 5 \text{ d}^{-1}$ ), with only faint (though significant) signals above that limit. The low-frequency signals consist in broad frequency groups, a narrow dominant peak, or a combination of features (a mix of isolated coherent signals and/or frequency groups). Red noise also appears to be frequent, as in other OB stars. Amplitudes of signals in periodograms often change over time, but the frequency content may also be altered. All these detected features are also observed in ‘normal’ Be stars, suggesting an absence of defining  $\gamma$  Cas characteristics in the optical photometric variability. Comparing the two recorded long-term variations of our sample with published cases, there does not seem to be a general rule (yet?) relating outburst occurrence and changing oscillation amplitudes in Be stars.

## ACKNOWLEDGEMENTS

The authors thank L. Eyser for valuable discussions on *Gaia* data, and J. Labadie-Bartz and J. Nichols for helping locate their published data. YN and GR acknowledge support from the Fonds National de la Recherche Scientifique (Belgium), the European Space Agency (ESA), and the Belgian Federal Science Policy Office (BELSPO) in the framework of the PRODEX Programme (contract HERMeS). AP acknowledges support from NCN grant no. 2016/21/B/ST9/01126. ADS and CDS were used for preparing this document.

Based on data obtained with the *TESS* mission, whose funding is provided by the NASA Explorer Program, as well as on archival data from *SuperWASP*, *BRITE*, *ASAS*, *ASAS-SN*, and on supporting *TIGRE* spectroscopy.

## DATA AVAILABILITY

The data underlying this article are available in repositories: *TESS* data are all available from the MAST archives, *ASAS*, *ASAS-SN*, *SuperWASP*, and *BRITE* data are also archived and available online – see footnotes 1, 2, 4, 5, 6, and 7 for details.

## REFERENCES

- Aerts C., Rogers T. M., 2015, *ApJ*, 806, L33  
 Balona L. A., Ozuyar D., 2020, *MNRAS*, 493, 2528  
 Blomme R. et al., 2011, *A&A*, 533, A4  
 Borre C. C. et al., 2020, *A&A*, 635, A140  
 Bowman D. M. et al., 2019, *Nat. Astron.*, 3, 760  
 Bowman D. M., Burssens S., Simón-Díaz S., Edelmann P. V. F., Rogers T. M., Horst L., Röpke F. K., Aerts C., 2020, *A&A*, 640, A36  
 Butters O. W. et al., 2010, *A&A*, 520, L10  
 Cameron C. et al., 2008, *ApJ*, 685, 489  
 Corben P. M., 1966, *MNASSA*, 25, 44  
 Cousins A. W. J., 1973, *MNASSA*, 32, 11  
 Dachs J., Lemmer U., 1989, *Astron. Gesellschaft Abstract Series*, 3, 61  
 Dougherty S. M., Taylor A. R., 1994, *MNRAS*, 269, 1123  
 Dubath P. et al., 2011, *MNRAS*, 414, 2602  
 Feinstein A., 1975, *PASP*, 87, 603  
 Feinstein A., Marraco H. G., 1979, *AJ*, 84, 1713  
 Hamaguchi K., Oskinova L., Russell C. M. P., Petre R., Enoto T., Morihana K., Ishida M., 2016, *ApJ*, 832, 140  
 Hameury J.-M., 2020, *Adv. in Space Res.*, 66, 1004  
 Heck A., Manfroid J., Mersch G., 1985, *A&AS*, 59, 63  
 Henry G. W., Smith M. A., 2012, *ApJ*, 760, 10  
 Huat A.-L. et al., 2009, *A&A*, 506, 95  
 Hubert A. M., Floquet M., 1998, *A&A*, 335, 565  
 Jernigan J. G., 1976, *IAU Circ.*, 2900, 1  
 Koen C., Eyser L., 2002, *MNRAS*, 331, 45  
 Labadie-Bartz J. et al., 2017, *AJ*, 153, 252  
 Labadie-Bartz J. et al., 2018, *AJ*, 155, 53  
 Lefèvre L., Marchenko S. V., Moffat A. F. J., Acker A., 2009, *A&A*, 507, 1141  
 Mahy L. et al., 2011, *A&A*, 525, A101  
 Mason K. O., White N. E., Sanford P. W., 1976, *Nature*, 260, 690  
 Miglio A., Montalbán J., Dupret M.-A., 2007, *Commun. Asteroseismol.*, 151, 48  
 Molenda-Zakowicz J., Polubek G., 2005, *Acta Astron.*, 55, 375  
 Moujtahid A., Zorec J., Hubert A. M., Garcia A., Burki G., 1998, *A&AS*, 129, 289  
 Nazé Y., Motch C., 2018, *A&A*, 619, A148  
 Nazé Y. et al., 2020a, *MNRAS*, 493, 2511  
 Nazé Y., Pigulski A., Rauw G., Smith M. A., 2020b, *MNRAS*, 494, 958  
 Nichols J. S. et al., 2010, *ApJS*, 188, 473  
 Olsen E. H., 1982, *A&AS*, 48, 165  
 Percy J. R., Hosick J., Kincaide H., Pang C., 2002, *PASP*, 114, 551  
 Percy J. R., Harlow C. D. W., Wu A. P. S., 2004, *PASP*, 116, 178  
 Pojmanski G., 1997, *Acta Astron.*, 47, 467  
 Pope B. J. S. et al., 2019, *ApJS*, 244, 18  
 Postnov K., Oskinova L., Torrejón J. M., 2017, *MNRAS*, 465, L119  
 Ramiamanantsoa T. et al., 2018, *MNRAS*, 473, 5532  
 Rauw G. et al., 2019, *A&A*, 621, A15  
 Rivinius T., Carciofi A. C., Martayan C., 2013, *A&AR*, 21, 69  
 Rivinius T., Baade D., Carciofi A. C., 2016, *A&A*, 593, A106  
 Rogers T. M., Lin D. N. C., McElwaine J. N., Lau H. B. B., 2013, *ApJ*, 772, 21

- Saio H., Kurtz D. W., Murphy S. J., Antoci V. L., Lee U., 2018, *MNRAS*, 474, 2774
- Semaan T., Hubert A. M., Zorec J., Frémat Y., Martayan C., Fabregat J., Eggenberger P., 2018, *A&A*, 613, A70
- Shappee B. J. et al., 2014, *ApJ*, 788, 48
- Smith M. A., Henry G. W., Vishniac E., 2006, *ApJ*, 647, 1375
- Smith M. A., Lopes de Oliveira R., Motch C., 2016, *Adv. Space Res.*, 58, 782
- Stagg C., 1987, *MNRAS*, 227, 213
- Stanishev V., Kraicheva Z., Boffin H. M. J., Genkov V., 2002, *A&A*, 394, 625
- Weiss W. W. et al., 2014, *PASP*, 126, 573
- Wichmann R., 2011, Astrophysics Source Code Library, record ascl:1106.016
- Zamanov R., Stoyanov K. A., Wolter U., Marchev D., Petrov N. I., 2019, *A&A*, 622, A173
- Zechmeister M., Kürster M., 2009, *A&A*, 496, 577

## APPENDIX A: V782 CAS

The light curve of V782 Cas is reminiscent of that of an eclipsing binary in an overcontact configuration. Assuming the Be star to be one of the components of that eclipsing binary leads, however, to a major contradiction. Indeed, TIGRE spectroscopic observations taken on 2019 November 1, November 18, and December 2 (i.e. immediately before, at the middle of, or immediately after the *TESS* campaign) clearly indicate a strong  $H\alpha$  emission line with an equivalent width between  $-24.1$  and  $-24.5 \text{ \AA}$ . The separation of the blue and red peaks varied between  $2.95$  and  $3.28 \text{ \AA}$ , corresponding to a separation in radial velocity of  $135\text{--}150 \text{ km s}^{-1}$ . Adopting  $v \sin i = 188 \text{ km s}^{-1}$  (see Nazé & Motch 2018, and references therein), relation (2) of Zamanov et al. (2019) for a Keplerian disc leads to  $R_{\text{disc}} \simeq 6.3 - 7.8 R_*$ . Hence, the Be star is surrounded by a wide decretion disc that is not compatible with the Be star being in an overcontact configuration. With  $\log L_{\text{bol}} = 4.15$  and  $T_{\text{eff}} = 19230 \text{ K}$  (Nazé & Motch 2018), we can estimate a stellar radius of  $10.7 R_\odot$ . Assuming a typical mass of  $10 M_\odot$  for the B2.5 IIIe star, we find that the semimajor axis of a binary system with a period of  $2.51 \text{ d}$  (corresponding to the detected frequency of  $\sim 0.4 \text{ d}^{-1}$ ) amounts to  $16.8(1+q)^{1/3} R_\odot$  where  $q$  is the mass ratio between the secondary and the B2.5 IIIe primary. Even at the hard limit of  $q \rightarrow 0.0$ , the radius of the Roche lobe remains below  $13 R_\odot$  that is totally inconsistent with the presence of a large circumstellar disc around the primary, unless the Be decretion disc would be circumbinary, which would make this system a very unusual case.

The most likely alternative then appears to be either a fortuitous line-of-sight alignment between the Be star and a short-period eclipsing binary or a genuine triple system consisting of the B2.5 IIIe star physically bound to the eclipsing binary. Concerning the first possibility, we have checked the *Gaia*-DR2 data base for contaminating sources within the 1 arcmin extraction radius of the *TESS* photometry. V782 Cas has a  $G$  magnitude of  $7.48$ . The next brightest object has  $G = 11.7$ , followed by stars with  $G \geq 12.9$ . Since the maximum depth of the primary eclipses amounts to  $0.02 \text{ mag}$ , whereas the secondary eclipses reach a depth of  $\sim 0.01 \text{ mag}$ , the eclipsing binary would contribute at least  $\sim 3$  per cent of the total light in the *TESS* photometry. If the *Gaia* and *TESS* photometric bands were identical, this result would imply that the line-of-sight object must be of magnitude  $G = 11.3$  or brighter. Taking into account the fact that the *TESS* band peaks at longer wavelengths than the *Gaia* band, the object at  $G = 11.7$  (*Gaia*-ID 515475966211949056) would be the most plausible candidate among the resolved neighbours.

To investigate this possibility, we folded the *TESS* data using  $T_0 = 2458790.7$  and  $P = 2.51256 \text{ d}$  and then built a light curve consisting of 100 normal points computed as the mean magnitude per  $0.01$  phase bin. We took the dispersion of the data points within a phase bin as our estimate of the uncertainty. We then used the `Nightfall` code (Wichmann 2011) to fit the light curve consisting of the normal points with a binary light curve model accounting for the presence of a third light and for reflection between the stars. Since the light curve fit is usually not very sensitive to the mass ratio, we fixed this parameter to unity. Lacking any information on the temperatures of the components of the eclipsing binary, we set the primary temperature to  $6000$  or  $10000 \text{ K}$ , and kept the secondary temperature as a fitting parameter. Setting the values of the third light (i.e. the Be star) contribution to values of 95 per cent and assuming Roche lobe filling factors below unity did not allow us to achieve an acceptable fit of the light curve. We thus tested overcontact configurations (i.e. values of the Roche lobe filling factor exceeding one). This improved the quality of the fit though there were still systematic deviations between the observational light curve and the model, and the best-fitting temperature of the secondary star became unrealistically low ( $< 100 \text{ K}$ ). We then allowed the code to adjust the value of the third light. This led to a significant improvement of the global adjustment, whilst simultaneously leading to lower values of the percentage of third light. For instance, the solution shown in Fig. A1 corresponds to Roche lobe filling factors of  $1.15$  for both stars, an inclination of  $27.9^\circ$ , primary and secondary temperatures of respectively  $10000$  and  $2600 \text{ K}$ , and a third light contribution of 75 per cent. This low value for the third light would imply that the eclipsing binary is not the neighbour with  $G = 11.7$ , rather suggesting a system unresolved from (hence possibly bound to) the Be star. We caution, however, that given the lack of constraints on the properties of the companions forming the eclipsing binary, there is certainly no unique solution. Our purpose here was only to check whether or not such an eclipsing binary scenario is plausible.

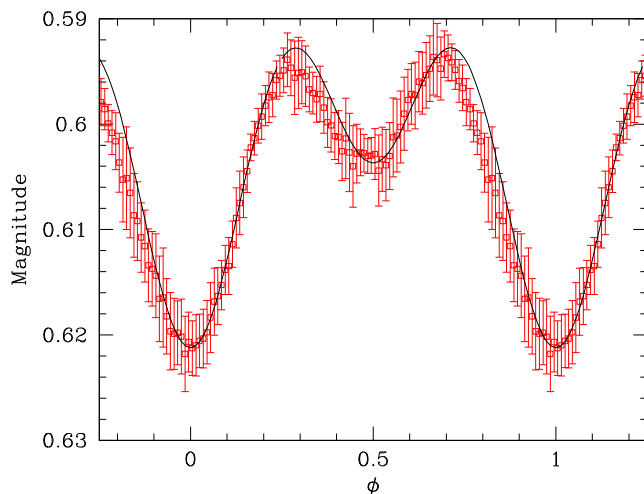


**Figure A1.** Binned *TESS* light curve (the red open rectangles) and best-fitting eclipse solution (see text for details).

This paper has been typeset from a  $\text{\LaTeX}$  file prepared by the author.